

Temperature Rise Caused by Shear Wave Elastography, Pulse Doppler and B-Mode in Biological Tissue: An Infrared Thermographic Approach

Maha Issaoui, Xavier Balandraud, Michel Grédiac, Benoît Blaysat, Lemlih × Ouchchane, Amelie Delabaere, Marie-Pierre Sauvant-Rochat, Didier Lemery

▶ **To cite this version:**

Maha Issaoui, Xavier Balandraud, Michel Grédiac, Benoît Blaysat, Lemlih × Ouchchane, et al.. Temperature Rise Caused by Shear Wave Elastography, Pulse Doppler and B-Mode in Biological Tissue: An Infrared Thermographic Approach. Ultrasound in Medicine & Biology, 2020, 46 (2), pp.325-335. 10.1016/j.ultrasmedbio.2019.10.008 . hal-03026025

HAL Id: hal-03026025
https://hal.science/hal-03026025

Submitted on 21 Jul 2022

HAL is a multi-disciplinary open access archive for the deposit and dissemination of scientific research documents, whether they are published or not. The documents may come from teaching and research institutions in France or abroad, or from public or private research centers.

L'archive ouverte pluridisciplinaire **HAL**, est destinée au dépôt et à la diffusion de documents scientifiques de niveau recherche, publiés ou non, émanant des établissements d'enseignement et de recherche français ou étrangers, des laboratoires publics ou privés.



Distributed under a Creative Commons Attribution - NonCommercial 4.0 International License

Version of Record: https://www.sciencedirect.com/science/article/pii/S0301562919315443
Manuscript_e478eef110bb0b15a6ef80d0eabd3a8e

Temperature rise caused by Shear Wave Elastography, Pulse-Doppler and B-mode in biological tissue: an infrared thermographic approach

Maha Issaoui[a], Xavier Balandraud[a], Michel Grédiac[a], Benoit Blaysat[a], Lemlih Ouchchane[b,c], Amelie Delabaere[b,d], Marie-Pierre Sauvant-Rochat[a,e], and Didier Lemery[b,d]

[a] Université Clermont Auvergne, CNRS, SIGMA Clermont, Institut Pascal, F-63000 Clermont-Ferrand, France

[b] Université Clermont Auvergne, CHU Clermont-Ferrand, CNRS, SIGMA Clermont, Institut Pascal, F-63000 Clermont-Ferrand, France

[c] Département de Santé Publique, Unité de Biostatistique et Informatique Médicale, CHU de Clermont-Ferrand, F-63000 Clermont-Ferrand, France

[d] Pôle Femme et Enfant, Centre Hospitalier Universitaire de Clermont-Ferrand, F-63000 Clermont-Ferrand, France

[e] Département de Santé Publique et Environnement, Université Clermont-Auvergne, UFR Pharmacie, F-63000 Clermont-Ferrand, France.

Address correspondence to: Maha Issaoui, Université Clermont Auvergne, CNRS, SIGMA Clermont, Institut Pascal, F-63000 Clermont-Ferrand, France. E-mail: maha.issaoui@etu.uca.fr

© 2019 published by Elsevier. This manuscript is made available under the CC BY NC user license
https://creativecommons.org/licenses/by-nc/4.0/

Abstract—The aim of the study is to demonstrate the interest and relevance of infrared thermography, which is a non-invasive full-field surface temperature measurement technique, to characterize the heterogeneous heating caused by ultrasound in biological tissue. Thermal effects of Shear Wave Elastography (SWE), Pulse-Doppler (PD) and B-mode were evidenced in porcine tissue. Experiments were performed using a high-frequency echography Aixplorer® system (Supersonic Imagine, Aix-en-Provence, France). For the three modes, ultrasound was applied continuously for 360 seconds while the temperature was recorded at the sample surface with a Cedip Jade III-MWIR infrared camera (Flir, Torcy, France). Temperature changes were detected for the three modes. In particular, “heat tunnels” crossing the sample were visualized from the early stages of the experiment. Heat conduction from the transducer was also involved in the global warming of the sample. The study opens up prospects for safety studies, potentially in addition to classical approaches such as those using thermocouples.

Keyword: Shear Wave Elastography; Ultrasound; Infrared thermography; Temperature rise; Safety

INTRODUCTION

Shear Wave Elastography (SWE) exploits acoustic radiation force (ARF) to generate stiffness maps in biological tissue. In practice, a 100 µs focused compression wave generates radiation force in dissipative biological media, which pushes the tissue for some dozens of µm in the target focal zone. When the tissue relaxes, it creates a shear wave propagating perpendicularly to the axis of the ultrasound beam at a speed of about 1 m/s. This shear wave is then visualized by ultrafast ultrasound imaging, capturing the wave front every 10 ms. Shear wave propagation speed is related to the Young's modulus of the biological tissue, a physical property usually expressed in kPa and characterizing material stiffness (Gennisson et al. 2013). The clinical relevance of SWE has been demonstrated for the detection of masses in superficial organs such as breast cancer (Cosgrove et al. 2012), and for the diagnosis of pathologies in deep organs, such as a cirrhotic liver (Guibal et al. 2016).

With the increasing number of publications on elastography, the World Federation for Ultrasound in Medicine and Biology (WFUMB) decided to take the initiative to create guidelines in August 2011. The first consensus meeting was held in March 2013 and led to the development of guidelines for basic science in elastography (Shiina et al. 2015), and for the use of this technique for the breast (Barr et al. 2015) and liver (Ferraioli et al. 2015), without distinguishing between the different elastography modes.

Elastography has recently been applied to gynecology (Thomas et al. 2007; Ami et al. 2009) and obstetrics (Kiliç et al. 2015; Alan et al. 2016; Quarello et al. 2016). Many published articles already deal with tissues that are accessible to methods necessitating the direct compression of the organ by the ultrasound probe, such as the cervix (Molina et al. 2012; Khalil et al. 2013; Hernandez-Andrade et al. 2014; Fruscalzo et al. 2016; O'Hara et al.

2018). Since SWE enables imaging without direct contact between the transducer and the observed tissue, it appears as the ideal candidate for fetal tissue elastography examinations (Diguisto et al. 2017; Mottet et al. 2017). However, until now there have been no guidelines on the use of SWE in obstetrics. Regardless of its clinical relevance, it is necessary to demonstrate its safety before allowing its utilization in routine practice for fetuses.

Diagnostic ultrasound can lead to two main types of potential effects on biological tissues, namely thermal and mechanical effects (Shankar and Pagel 2011a). The thermal effect was for instance studied by Palmeri and Nightingale (2004) using thermocouples placed inside the tissue (Palmeri et Nightingale 2004). It is important to note that the period of organogenesis is considered as particularly sensitive to thermal stress (Fowlkes 2008). Investigations on laboratory animals have documented that an elevation in temperature can damage biological tissues (Pellicer et al. 2011; Schneider-Kolsky et al. 2009). Thermally-induced teratogenesis has been shown in many animal studies (Germain et al.1985). The issue of temperature rise due to ultrasound, and SWE in particular, is thus critical.

In the present work, we focus on the observation of the thermal effect in biological tissue generated by three ultrasonic modes, namely SWE, Pulse-Doppler (PD) and B-mode. An infrared (IR) thermographic camera was used for this purpose. This device provides full-field temperature measurements at the surface of the object under investigation. In the last few decades, IR thermography has become widespread in the mechanics of materials community, leading to important insights into the thermal response of materials subjected to mechanical excitation (Chrysochoos et al. 2010). It is in particular possible to experimentally evidence thermo-mechanical couplings, i.e. temperature variations caused by changes in the mechanical state of the material. Various mechanical phenomena in various materials are related to calorific responses, for instance elasticity, plasticity, viscosity, fatigue damage, elasto-plastic transition, cracking, vibrations, friction, strain- or stress-induced phase transitions, etc. IR

thermography is now recognized as a relevant experimental means to study the thermomechanics of materials. However, to the best of the authors' knowledge, thermographic approaches have not before been applied to the calorific response of biological tissues subjected to ultrasonic excitation.

The aim of the present study is to demonstrate the interest and the relevance of IR thermography to characterize the heterogeneous heating caused by ultrasound in biological tissue. Two modalities which are already authorized for pregnant women (PD and B-mode) were compared with the SWE mode, with potential perspectives for the study of the safety of the latter in obstetrics (Issaoui et al. 2018).

MATERIALS AND METHODS

Experimental setup

The echography system used for the experiments was a high-frequency Aixplorer® (Supersonic Imagine, Aix-en-Provence, France). It features three imaging modes: B-Mode, PD and SWE. The chosen transducer, typically used in obstetrics, was a curved SC6-1 probe (Supersonic Imagine, Aix-en-Provence, France) featuring 192 piezoelectric elements and a bandwidth of 1-6 MHz. Temperature measurements were carried out using a Cedip Jade III-MWIR camera (Flir, Torcy, France). This IR camera features a wavelength range of 3.5-5 μm, a sensor size of 320×240 pixels and a Noise Equivalent Temperature Difference (NETD) equal to 0.02°C. This latter quantity corresponds to the temperature measurement resolution, that is, the change in quantity being measured that causes a change in the corresponding indication of greater than one standard deviation of the measurement noise (Chrysochoos and

Surrel 2012). The lower the measurement resolution, the lower the noise and thus the better the measurement.

Measurements were performed on homogeneous pieces of porcine muscle (slaughterhouse: Hassenforder et fils S.A.S., Vichy, France; identification number: 11P18025; FR-03-094-001 CE; order number; CV18032542) by three operators (MI, XB and DL). Several samples with dimensions of 130×70×60 mm^3 were cut by hand. Two configurations were tested in terms of the location of the transducer with respect to the porcine sample (Fig. 1-a). The reason for this positioning on the sample was that IR thermography provides temperature maps at the surface of the observed object. In Configuration #1, the surface observed by the IR camera is perpendicular to the plane of the transducer, whereas it is parallel to it in Configuration #2. The two test configurations were considered as complementary in order to obtain two perpendicular slices of the three-dimensional temperature field in the bulk. It is worth noting that air is a bad conductor of heat by natural convection, while pig muscle transmits heat relatively well by conduction (thermal diffusivity of 1.14E-7 m^2/s (Giering et al. 1995). Temperature rises during experiments are expected to be overestimated compared to a situation for which the dimensions of the sample were infinite.

A second sample was used as a reference to track thermal fluctuations in the close environment (Fig. 1-b). The sample to be subjected to ultrasound (named “sample” in the following) and the reference sample (named “reference” in the following) were placed in a homemade plastic frame featuring two shelves. The reference was placed under the sample, in the IR camera’s field of view. The bottom part of the transducer was also visible at the top of the thermal images. Note that the reference was placed close enough to the sample so that it can be reasonably assumed that it was submitted to the same environmental fluctuations

during testing. However, the reference was physically separate from the sample, so it was not affected by ultrasonic excitation.

Figure 1-c shows three photographs of the experiment. The transducer was in contact with the sample using a static system ensuring a constant force. The sample was therefore deformed in addition to the effect of gravity. It is worth noting that performing quantitative measurements with an IR camera is somewhat tricky when temperature changes are small. This is due to the fact that various phenomena potentially influence the measured temperatures in addition to the desired ones, for instance potential changes in the ambient airflow or in ambient temperature, and more generally in the elements inside the testing room (persons, heating system, doors opened, etc.). Misleading conclusion could therefore be drawn from measured temperature fields if some precautions are not taken when preparing and performing the tests. First, a cardboard tunnel was placed between the IR camera and the observed surfaces. Second, attention was paid to ensure the steady thermal state of the testing room. To this end, the echography system, IR camera and computers were turned on three hours before the test session began, and nobody was present in the room during the tests, in order to limit airflow. No operator was required to maintain the transducer/sample contact thanks to the use of a fixed gripping system. Operators left the room just after starting the test, whose end was programmed automatically. Thermal acquisition began twenty seconds before starting ultrasonic excitation. Synchronization uncertainty was of about 0.5 s because of the thermal recording frequency f_{R} set to 2 Hz, which is acceptable when considering the response time of the thermal phenomena and the test duration.

The three echography modes (B-mode, PD and SWE) were applied for comparison purposes, using a gel for the coupling between sample and transducer. Table 1 provides the ultrasound parameters for each mode. For the three modes, the ultrasonic excitation ran continuously for 360 s and then stopped. For each test, the IR camera measurements lasted

longer than this, so that temperature variations could be monitored after the ultrasonic activity had stopped. A waiting time of one hour was respected between two consecutive tests, to ensure a thermal steady state when starting the second one. Note that for the B-mode, two focal configurations were also compared (10-25 mm and 25-40 mm), but preliminary tests showed that there was no difference in terms of temperature distributions, probably due to low calorific impact in both cases. Finally, the spatial resolution of the measured temperature maps was 0.53 mm. In the metrological framework of full-field measurement techniques, the spatial resolution can be defined as the period of the sine quantity beyond which the relative loss in amplitude of the quantity returned by the measuring technique is greater than a certain value (Grédiac et al. 2017). Basically, the spatial resolution can be seen as the shortest distance between two spatially independent measurements. For raw thermal data provided by an IR camera featuring independent sensors, the spatial resolution is equal to the pixel size projected on the surface under investigation. Each temperature map can thus be seen as a grid of "thermocouples" with a pitch equal to 0.53 mm.

Measurement of temperature change due to ultrasonic excitation

The calibration of the temperature measurement was performed by XB using a SR-800-7D extended area blackbody (CI-systems) with a two-point procedure (10°C and 35°C) and an integration time of 1500 µs. The thermal emissivity of the biological tissue was considered to be equal to 0.95, with an environment temperature corresponding to the ambient temperature (between 24°C and 26°C over the whole duration of the test period). The thermal emissivity value was defined after preliminary tests comparing temperature changes with and without covering the raw surface of the biological tissue with matt black paint. Results evidenced the high thermal emissivity of the raw surface of the sample. Two precautions were

taken to ensure the correct assessment of the temperature changes due to ultrasound: (i) the use of specific thermal acquisition conditions to reduce noise, and (ii) the subtraction of thermal fluctuations in the environment thanks to the reference.

(i) The IR camera acquisition frequency f_A was set to 100 Hz, but each recorded image was the average of 50 successive frames, thus leading to a recording frequency f_R of 2 Hz. This setting was chosen based on preliminary tests (not detailed here) which showed that the temperature change is smooth enough whatever echography mode is chosen. Indeed, no "sudden" temperature increase could be observed. Averaging enables us to improve measurement resolution compared to the base NETD of the IR camera, but without losing information (see for instance (Gonzales and Woods 2006)). In theory, for Gaussian noise, the temporal averaging operation of 50 frames improves the measurement resolution by a factor of $\sqrt{50}$ but this impairs the temporal resolution. Applying this procedure leads the standard deviation of the resulting noise to be equal to some thousandths of one degree only.

(ii) Figure 2 illustrates the interest of using the reference for the correct assessment of the temperature change due to ultrasound only. The data correspond here to a test performed in Configuration #1 for the B-mode. The black curve shows the temperature change of the reference, while the blue one shows the temperature at point A on the sample subjected to ultrasound (see schematic view in Figure 2 for the location of point A). By "point", we mean the surface element on the sample plane corresponding to one pixel, whose dimension is 0.53×0.53 mm^2. Note that the measurement resolution of the reference temperature was improved by spatially averaging over a large rectangular zone (see schematic view in Figure 2). The red curve corresponds to the temperature change at point A due to ultrasonic waves only, obtained by subtracting the temperature change of the reference from that of the sample. Even if fluctuations in the environment (black curve) were limited to a few hundredths of a degree, it can be seen that the raw data at point A slightly underestimates the data to be

considered for the analysis (the blue curve is below the red one). It is worth noting that the "strong" perturbation around time 120 s was correctly removed by the processing.

RESULTS

For the sake of clarity, physical measurements are commented in the present section while the clinical impact is developed in the following one.

Analysis of some temperature change maps

Figure 3 presents the maps of temperature change at t = 80 s in Configuration #1 for the three echography modes. This specific time was selected to highlight the *remote* heating from the transducer. The following comments can be drawn from this figure:

- for the three modes, a vertical "heat tunnel" is visible under the contact with the transducer (see the arrows in the images). This phenomenon cannot be explained by an increase in the transducer temperature accompanied by heat conduction inside the sample. Indeed, assuming isotropic thermal conduction in the tissue, a concentric distribution would have been obtained if only heat conduction was involved. Note, however, that a conduction effect can be observed just under the contact with the transducer, especially for the SWE mode (see green color in Fig. 3-c). This is a consequence of the self-heating of the piezoelectric elements themselves;
- the vertical tunnels appear to be quite homogeneous in temperature for both the B-mode (Fig. 3-a) and PD (Fig. 3-b): see homogeneous green color corresponding to a temperature change lying between about 0.04°C and 0.06°C. For SWE, hotter zones are clearly visible at the bottom part and some centimeters under the contact with the

transducer (Fig. 3-c). This latter observation confirms the *remote* heating from the transducer, which is due to the ultrasonic waves crossing the sample in the plane of the transducer. The hot zone at the bottom part can be explained by a reflection of the waves, whereas the hot zone under the contact with the transducer can be explained by an effect of beam focusing. This second hot zone appears to be located about 20 mm under the contact with the transducer in the observation plane, to be compared with the focal zone of 25-40 mm given in Table 1. The difference can be explained by recalling that the transducer is curved. The hot zone is probably also curved inside the sample, explaining the measurement of 20 mm in the observation plane;

- in order to have better color dynamics for each mode individually, Figure 3-d shows some close-up views of the central zone with suitable color scales. With these representations, reflections at the bottom part of the sample are also visible for the B-mode. Clearly, the caloric effect of SWE in the biological tissue is greater than that of both B-mode and PD.

As a general conclusion from Figure 3, the three heat tunnels in the temperature change maps constitute a clear signature of remote heating from the transducer, associated with wave propagation.

Figure 4 presents the thermal maps obtained for Configuration #1 at the end of transducer activation, i.e. at t = 360 s. For B-mode and PD (Figs. 4-a and -b), the color scales are the same as in Figure 3, for comparison purposes. For SWE, the color scale was modified because of the much stronger thermal activity for this mode. As a first comment, the heat tunnels can again be observed, but they appear thicker compared to those obtained at t = 80 s (Fig. 3). Moreover, their widths are not homogeneous: they are indeed larger at their ends (close to the transducer and at the bottom). This can be explained by heat conduction inside the tissue: the heat that was created *remotely* by the waves progressively diffused. As a

general comment, temperature distribution is the result of three causes: the heat source produced by wave propagation, heat conduction inside the tissue, and the heat exchanged with the sample environment (by convection with ambient air and by contact with both the frame and the transducer).

Figure 5 presents the temperature change maps for t =360 s for Configuration #2 and for the three echography modes. The magnitude of temperature increase is globally greater than for Configuration #1 at the same time (see Figure 4). The link between the data for the two configurations will be discussed in the next section. In the measurement plane observed with Configuration #2, the highest temperature changes in the sample are located close to the transducer, which can be explained by heat transfer through contact. Heat tunnels similar to those observed for Configuration #1 are visible, although they are more difficult to visualize (dark blue).

It is worth noting that such features can only be observed and quantified thanks to a full-field thermal measurement technique.

Analysis of the temperature time variation

Figure 6 shows the temperature change as a function of time at two points A and B, for Configurations #1 and #2 respectively, for the three echography modes. The locations of these points were chosen because they correspond to the most intense heating zones. The vertical dashed lines correspond to the end of transducer activation, i.e. at time t = 360 s. Several comments can be made with respect to this figure:

- SWE generates greater temperature changes for both configurations. PD causes a larger increase in temperature than B-mode. This result is in agreement with previous studies, see Ref. (Miloro et al. 2017) for instance. The difference in noise level

between Configurations #1 or #2 might be explained by the small movements of the physical points observed by the IR camera at the specimen surface. Such movements can potentially be due to oscillations caused by mechanical waves. The noise level would thus depend on the orientation of the surface observed (Configurations #1 or #2) with respect to the wave plane;

- for Configuration #2, the temperature clearly still increases for several tens of seconds after halting the ultrasonic excitation (Fig. 6-b). This phenomenon can be explained by the fact that heat is still transferred from the "hot" transducer. This confirms that, in addition to *remote* heating, heat conduction is also involved;
- as indicated in the "Materials and methods" section, Configurations #1 and #2 were initially considered as complementary, to obtain two perpendicular slices of the tri-dimensional temperature field in the bulk. This approach appears to be reasonable when comparing Figures 6-a and 7. The latter presents the temperature change as a function of time for another point (named C) in Configuration #2. This point is at the same location with respect to the transducer as point A in Configuration #1: see the schematic view at the top of Figure 7. At time t = 360 s for the B-mode, the temperature increase is nearly equal to 0.3°C for both Configurations #1 and #2 (compare the green curves in Figures 6-a and 7), thus validating the approach. Similarly, the temperature increase for PD at t = 360 s is nearly equal to 0.4°C for both configurations (compare the blue curves in Figures 6-a and 7);
- a specific remark can be made concerning the SWE mode. At t = 360 s, the temperature change is nearly equal to 1.17°C for both configurations (compare the red curves in Figures 6-a and 7), but the temperature continues to increase in Configuration #2 after t = 360 s, reaching 1.56°C. This difference between the two curves can be explained by the fact that points A and C are not exactly equivalent. For

instance, it can be noted that the hatched zone in Configuration #2 is not present in Configuration #1 (Fig. 7). This effect of thermal inertia is also visible in Figure 7 for both PD and B-mode, even if it is less pronounced than for SWE. The delay before starting the return to ambient temperature can be explained by a competition between heat loss by convection with the ambient air and heat absorption by contact with the transducer. The latter is hotter than the tissue, and thus transfers heat to it.

Finally, Figures 8, 9 and 10 provide the temperature change as a function of time for the B-mode, PD and SWE respectively, at various points and for both configurations. The location of these points is reported in Figure 8-a for Configuration #1 and in Figure 8-b for Configuration #2. Point P1 corresponds to point A in Figure 6-a (Configuration #1), while Point P8 corresponds to point B in Figure 6-b (Configuration #2). An additional point (P0) was directly placed on the transducer in Configuration #2, enabling us to capture the highest temperature change in the thermal scene. It can be observed that, at the end of the ultrasonic excitation (at t = 360 s), the temperature of the transducer reaches 0.95°C for the B-mode and PD, and 1.95°C for SWE. Close to the transducer, heat conduction by contact is not negligible. Note that the noise in the curves in Figures 8-a (B-mode in Configuration #1) and 9-a (PD in Configuration #1) appears to be greater than in the other curves, merely because of the scale used for the y-axis. As already noted above, B-mode and PD are less calorific than SWE.

DISCUSSION

Elastography, including SWE, is commonly used in various clinical applications (Cosgrove et al. 2012; Guibal et al. 2016). Potential indications of SWE in fetal and uterine imaging during

pregnancy are cervix examination (Fruscalzo et al. 2016), and more importantly the monitoring of fetal development. Recently, SWE was used to explore the fetal brain (Diguisto et al. 2017) and lung (Mottet et al. 2017). In these studies, the authors considered that the benefit-to-risk ratio of this technique was favorable. However, a recent review was unable to demonstrate the safety of SWE regarding the fetus (Issaoui et al. 2018). Palmeri and Nightingale (2004), Nitta et al. (2001) and Bouchard et al. (2009) studied the temperature rise created by ARF in soft tissue (porcine muscle) by using thermocouples (Palmeri et Nightingale 2004; Bouchard et al. 2009; Nitta et al. 2015). Skurczynski et al. (2009) analyzed the temperature increase and the cavitation effect by performing focused diagnostic ultrasound: they reported a potential heating risk during elasticity measurement by ARF when a bone is present (Skurczynski et al. 2009). The effect of temperature rise potentially leading to the teratogenesis of developing tissues was evidenced *in vivo* in animal models. This effect is documented in Refs (Hinoue et al. 2001; Church and Miller 2007; Abramowicz et al. 2008; Shankar and Pagel 2011b). Abnormalities include growth retardation, microencephaly, cataract, and other malformations (Ziskin and Morrissey 2011). Some *in vivo* experiments have also shown that the threshold temperature increase for teratogenic effects induced by hyperthermia is estimated at 1.5°C for an exposure of 5 min (Abramowicz 2002; Abramowicz et al. 2008). A major problem with formulating hypotheses from animal data is that *in vivo* effects of hyperthermia seen in animals result from exposure situations that would never be encountered by the human embryo or fetus during ultrasound examination. However, a review of the literature by Marinac-Dabic et al. (2002) identified the epidemiologic studies focusing on human exposure to diagnostic ultrasound during pregnancy and the potential associations between *in utero* ultrasound exposure and growth restriction, delayed speech, dyslexia and non-right-handedness. The authors concluded that there was no association between *in utero* exposure to ultrasound and either growth restriction or delayed speech. There are,

363 nonetheless, some questions about non-right-handedness after frequent exposure to Doppler
364 ultrasound. However, no definitive conclusions can yet be drawn. To date no study has
365 specifically looked at the effects of SWE.

366 In this context, developing experimental techniques to measure the temperature rise in
367 biological tissue caused by ultrasound is of prime interest. Thermocouples placed inside the
368 tissue are classically employed and have proved to be efficient. The present study shows that
369 IR thermography could be a complementary experimental approach. This technique provides
370 temperature maps without contact with the tissue, thus avoiding the potential artefacts that
371 thermocouples may cause. Indeed, since ARF creates a matter displacement, it is difficult to
372 know to what extent a thermocouple will generate a secondary ultrasound source (thus
373 creating a secondary heat source).

374 A limitation of our study is that it was performed on samples containing only soft
375 tissues: our samples did not contain bone parts. Many other studies have shown that the
376 thermo-sensitivity of bone is much higher than that of soft tissues (Skurczynski et al. 2009;
377 Nitta et al. 2015; Tabaru et al. 2012). In fact, a fetus is composed principally of soft tissues
378 but also of bones. For obvious ethical reasons however, it was impossible to perform these
379 tests on fetal tissues. Further studies should be performed on phantoms containing soft tissues
380 and bones.

381 The strength of the present test procedure is that precautions were taken to avoid
382 potential misinterpretation of the results: a waiting time before starting any new test from an
383 initial thermal steady state, the subtraction of parasitic effects thanks to a reference sample,
384 and noise reduction. It can be noted that, as usual for full-field measurement techniques, huge
385 amounts of data were recorded (videos of several hundreds of megabytes for each test) and
386 processed. After preliminary tests, the experiments were repeated twice in order to check that
387 the results were similar. Let us recall that the objective of the study was not to perform a

statistical analysis of the results, but to demonstrate the relevance of IR thermography as an experimental tool for the study of temperature increases due to ultrasound use.

Some final comments can be advanced about the material used for the test. Porcine muscle was chosen because it has well-characterized acoustic and thermal properties, similar to those reported for clinically relevant human soft tissues (Liang et al. 1991). There are problems in relating laboratory animal studies to humans. We cannot extrapolate to humans the results of studies performed on animals, or even from one animal species to another, because differences in the results and conclusions may be due to strain differences.

CONCLUSION

SWE is a recent diagnostic ultrasound modality offering the possibility of a quantitative assessment of tissue elasticity. It may have numerous potential applications in obstetric and fetal imaging. The present study demonstrated the benefit of using surface temperature maps captured by an IR camera for the analysis of heterogeneous heating caused by ultrasound. The temperature rise in SWE mode appeared to be much higher compared to the other two modes under study (B-mode and PD), as has already been indicated in thermocouple-based studies. The IR thermography technique, in parallel with the thermocouple approach, could advantageously be employed to study the safety of SWE in obstetrics. Tests on samples containing both soft tissues and bones are also a perspective of this study. Finally, future works could also concern the coupling of IR thermography with thermocouples placed inside a phantom imitating biological tissue, in order to potentially reconstruct the variations in the entire three-dimensional temperature field accompanying ultrasound.

ACKNOWLEDGEMENTS

The authors would like to thank Dr. Piero Miloro from National Physical Laboratory (NPL), UK for the fruitful discussions about temperature rises due to elastography in tissues.

REFERENCES

Abramowicz JS. Ultrasound in obstetrics and gynecology: Is this hot technology too hot? J Ultrasound Med 2012;21(12):1327–33.

Abramowicz JS, Barnett SB, Duck FA, Edmonds PD, Hynynen KH, Ziskin MC. Fetal thermal effects of diagnostic ultrasound . J Ultrasound Med 2008;27(4):541–59.

Alan B, Goya C, Tunç S, Teke M, Hattapoğlu S. Assessment of placental stiffness using acoustic radiation force impulse elastography in pregnant women with fetal anomalies. Korean J Radiol 2016;17(2):218–23.

Ami O, Lamazou F, Mabille M, Levaillant JM, Deffieux X, Frydman R, Musset D. Real-time transvaginal elastosonography of uterine fibroids. Ultrasound Obstet Gynecol 2009;34(4):486–88.

Barr RG, Nakashima K, Amy D, Cosgrove D, Farrokh A, Schafer F, Bamber JC, Castera L, Choi BI, Chou YH, Dietrich CF, Ding H, Ferraioli G, Filice C, Friedrich-Rust M, Hall TJ, Nightingale KR, Palmeri ML, Shiina T, Suzuki S, Sporea I, Wilson S, Kudo M. WFUMB guidelines and recommendations for clinical use of ultrasound elastography: Part 2: breast. Ultrasound Med Biol 2015;41(5):1148–60.

Bouchard RR, Dahl JJ, Hsu SJ, Palmeri ML, Trahey GE. Image quality, tissue heating, and frame rate trade-offs in acoustic radiation force impulse imaging. IEEE Trans Ultrason Ferroelectr Freq Control. 2009;56(1):63–76.

437 Chrysochoos A, Huon V, Jourdan F, Muracciole JM, Peyroux R, Wattrisse B. Use of full-
438 field digital image correlation and infrared thermography measurements for the
439 thermomechanical analysis of material behaviour. Strain 2010;46(1):117–130
440 Chrysochoos A and Surrel Y. Basics of metrology and introduction to techniques. In: Grediac
441 M and Hild F (Eds) Full-field measurements and identification in solid mechanics,
442 Wiley-ISTE, 2012. pp. 1–29
443 Church CC and Miller WM. Quantification of risk from fetal exposure to diagnostic
444 ultrasound. Prog Biophys Mol Biol 2007;93(1):331–53.
445 Cosgrove DO, Berg WA, Doré CJ, Skyba DM, Henry JP, Gay J, Cohen-Bacrie C. Shear wave
446 elastography for breast masses is highly reproducible. Eur Radiol 2012;22(5):1023–32.
447 Diguisto C, Simon EG, Callé S, Ternifi R, Remeniéras JP, Hervé P, Perrotin F. Ultrasonic
448 elastography exploration of the foetal brain: a case of atypical choroid plexus papilloma. J
449 Obstet Gynaecol 2017;37(4):525–27.
450 Ferraioli G, Filice C, Castera L, Choi BI, Sporea I, Wilson SR, Cosgrove D, Dietrich CF,
451 Amy D, Bamber JC, Barr R, Chou YH, Ding H, Farrokh A, Friedrich-Rust M, Hall TJ,
452 Nakashima K, Nightingale KR, Palmeri ML, Schafer F, Shiina T, Suzuki S, Kudo M.
453 WFUMB guidelines and recommendations for clinical use of ultrasound elastography:
454 Part 3: liver. Ultrasound Med Biol 2015;41(5):1161–79.
455 Fowlkes JB. American institute of ultrasound in medicine consensus report on potential
456 bioeffects of diagnostic ultrasound. J Ultrasound Med 2008;27(4):503–15.
457 Fruscalzo A, Mazza E, Feltovich H, Schmitz R. Cervical elastography during pregnancy: a
458 critical review of current approaches with a focus on controversies and limitations. J Med
459 Ultrason 2016;43(4):493–504.
460 Gennisson JL, Deffieux T, Fink M, Tanter M. Ultrasound elastography: Principles and
461 techniques. Diagn Interv Imaging 2013;94(5):487–95.

462 Germain MA, Webster WS, Edwards MJ. Hyperthermia as a teratogen: parameters
463 determining hyperthermia-induced head defects in the rat. Teratology 1985;31(2):265–
464 72.
465 Giering K, Minet O, Lamprecht I, Müller G. Review of thermal properties of biological
466 tissues. SPIE PM 1995;25:45–65
467 Gonzales RC and Woods RE. Digital Image Processing, third ed. Upper Saddle River, NJ:
468 Prentice-Hall, 2006
469 Grédiac M, Blaysat B, Sur F. A critical comparison of some metrological parameters
470 characterizing local Digital Image Correlation and Grid Method. Exp Mech
471 2017;57(6)871–903
472 Guibal A, Renosi G, Rode A, Scoazec JY, Guillaud O, Chardon L, Munteanu M, Dumortier J,
473 Collin F, Lefort T. Shear wave elastography: An accurate technique to stage liver fibrosis
474 in chronic liver diseases. Diagn Interv Imaging 2016;97(1):91–99.
475 Hernandez-Andrade E, Aurioles-Garibay A, Garcia M, Korzeniewski SJ, Schwartz AG, Ahn
476 H, Matinez-Varea A, Yeo L, Chaiworapongsa T, Hassan SS, Romero R. Effect of depth
477 on shear-wave elastography estimated in the internal and external cervical os during
478 pregnancy. J Perinat Med 2013;42(5):549–57.
479 Hinoue A, Fushiki S, Nishimura Y, Shiota K.In utero exposure to brief hyperthermia
480 interferes with the production and migration of neocortical neurons and induces apoptotic
481 neuronal death in the fetal mouse brain. Brain Res Dev Brain Res 2001;132(1):59–67.
482 Issaoui M, Debost-Legrand A, Skerl K, Chauveau B, Magnin B, Delabaere A, Boyer L,
483 Sauvant-Rochat MP, Lémery D. Shear wave elastography safety in fetus: a quantitative
484 health risk assessment. Diagn Interv Imaging 2018;99(9):519–24.
485 Khalil MR, Thorsen P, Uldbjerg N. Cervical ultrasound elastography may hold potential to
486 predict risk of preterm birth. Dan Med J 2013;60(1):A4570.

487 Kiliç F, Kayadibi Y, Yuksel MA, Adaletli I, Ustabaşıoglu FE, Oncul M, Madazli R, Yılmaz
488 MH, Mihmanli I, Kantarci F. Shear wave elastography of placenta: in vivo quantitation of
489 placental elasticity in preeclampsia. Diagn Interv Radiol 2015;21(3):202–7.
490 Liang XG, Ge XS, Zhang YP, Wang GJ. A convenient method of measuring the thermal
491 conductivity of biological tissue. Phys Med Biol 1991;36(12):1599–1605.
492 Marinac-Dabic D, Krulewitch CJ, Moore RM Jr. The safety of prenatal ultrasound exposure
493 in human studies. Epidemiology 2002;13 Suppl 3:S19–22.
494 Miloro P, Eleanor M, Adam S. Temperature elevation measured in a tissue-mimicking
495 phantom for transvaginal ultrasound at clinical settings. Ultrasound 2017;25(1):6–15.
496 Molina FS, Gómez LF, Florido J, Padilla MC, Nicolaides KH. Quantification of cervical
497 elastography: a reproducibility study. Ultrasound Obstet Gynecol 2012;39(6):685–89.
498 Mottet N, Aubry S, Vidal C, Boiteux G, Metz JP, Riethmuller D, Pazart L, Ramanah R.
499 Feasibility of 2-D ultrasound shear wave elastography of fetal lungs in case of threatened
500 preterm labour: a study protocol. BMJ Open 2017;7(12):e018130.
501 Nitta N, Ishiguro Y, Sasanuma H, Taniguchi N, Akiyama I. Experimental system for in-situ
502 measurement of temperature rise in animal tissue under exposure to acoustic radiation
503 force impulse. J Med Ultrason (2001) 2015;42(1):39–46.
504 O'Hara S, Zelesco M, Sun Z. Shear wave elastography on the uterine cervix: technical
505 development for the transvaginal approach. J Ultrasound Med 2018;
506 https://doi.org/10.1002/jum.14793
507 Palmeri ML and Nightingale KR. On the thermal effects associated with radiation force
508 imaging of soft tissue. IEEE Trans Ultrason Ferroelectr Freq Control 2004;51(5):551–65.
509 Pellicer B, Herraiz S, Táboas E, Felipo V, Simon C, Pellicer A. Ultrasound bioeffects in rats:
510 quantification of cellular damage in the fetal liver after pulsed doppler imaging.
511 Ultrasound Obstet Gynecol 2011;37(6):643–48.

512 Quarello E, Lacoste R, Mancini J, Melot–Dusseau S, Gorincour G. Shear wave elastography
513 of fetal lungs in pregnant baboons. Diagn Interv Imaging 2016;97(6):605–10.
514 Schneider-Kolsky ME, Ayobi Z, Lombardo P, Brown D, Kedang B, Gibbs ME. Ultrasound
515 exposure of the foetal chick brain: effects on learning and memory. Int J Dev Neurosci
516 2009;27(7):677–83.
517 Shankar H and Pagel PS. Potential adverse ultrasound-related biological effects: a critical
518 review. Anesthesiology 2011;115(5):1109–24.
519 Shiina T, Nightingale KR, Palmeri ML, Hall TJ, Bamber JC, Barr RG, Castera L, Choi BI,
520 Chou YH, Cosgrove D, Dietrich CF, Ding H, Amy D, Farrokh A, Ferraioli G, Filice C,
521 Friedrich-Rust M15, Nakashima K, Schafer F, Sporea I, Suzuki S, Wilson S, Kudo M.
522 WFUMB guidelines and recommendations for clinical use of ultrasound elastography:
523 Part 1: basic principles and terminology. Ultrasound Med Biol 2015;41(5):1126–47.
524 Skurczynski MJ, Duck FA, Shipley JA, Bamber JC, Melodelima D. Evaluation of
525 experimental methods for assessing safety for ultrasound radiation force elastography.
526 Brit J Radiol 2009;82(980):666–74.
527 Tabaru M, Yoshikawa H, Azuma T, Asami R, Hashiba K. Experimental study on temperature
528 rise of acoustic radiation force elastography. J Med Ultrason (2001) 2012;39(3):137–46.
529 Thomas A, Kümmel S, Gemeinhardt O, Fischer T. Real-time sonoelastography of the cervix:
530 tissue elasticity of the normal and abnormal cervix. Acad Radiol 2007;14(2):193–200.
531 Ziskin MC and Morrissey J. Thermal thresholds for teratogenicity, reproduction, and
532 development. Int J Hyperthermia 2011;27(4):374–87.
533

Figure captions list

Fig. 1 Experimental setup: a) two tested configurations, b) schematic views of Configuration #1, c) photographs of the experiment involving a curved transducer.

Fig. 2. Illustration of the benefit of using the reference sample. Data correspond here to a test performed in Configuration #1 for B-mode.

Fig. 3. Maps of temperature change at t =80 s for Configuration #1: a) B-mode, b) PD, c) SWE. The color scale is the same as in Figs. 4-a and -b for comparison purposes. d) Snapshots of the central zone with suitable color scales.

Fig. 4. Maps of temperature change at t = 360 s for Configuration #1: a) B-mode, b) PD, c) SWE.

Fig. 5. Maps of temperature change at t = 360 s for Configuration #2: a) B-mode, b) PD, c) SWE.

Fig. 6. Temperature change at points A and B for a) Configuration #1 and b) Configuration #2, respectively. The vertical dashed lines correspond to the end of transducer activation.

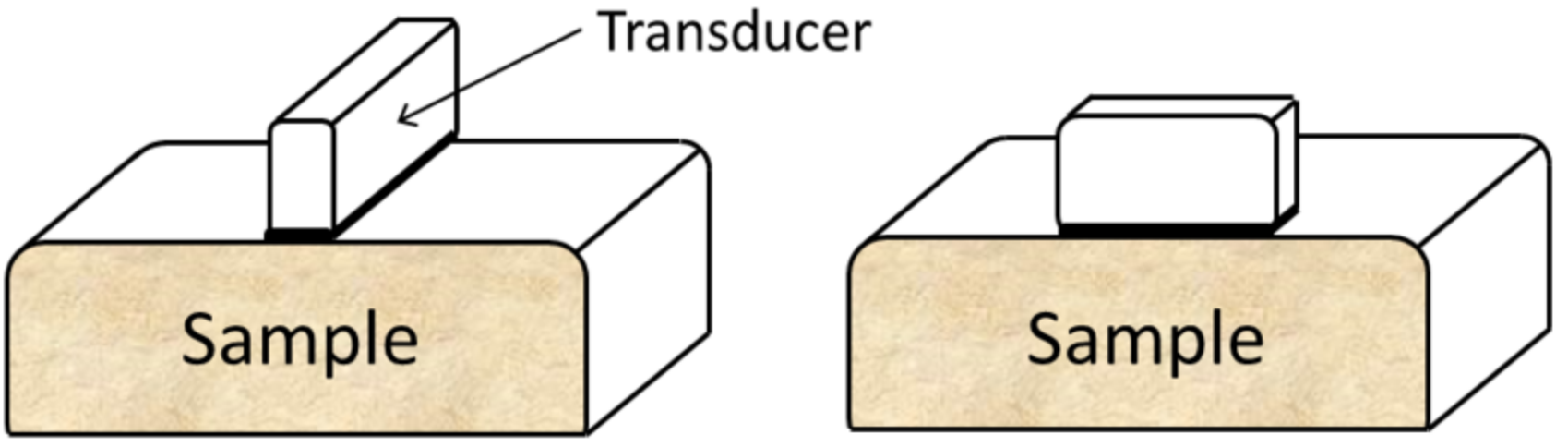
Fig. 7. Temperature change at point C for Configuration #2, for comparison purposes with point A in Configuration #1 (compare with in Fig. 6-a). The vertical dashed line corresponds to the end of transducer activation. The hatched area corresponds to the part of the sample which is not present in Configuration #1.

Fig. 8. B-mode: a) temperature change as a function of time in Configuration #1, b) same in Configuration #2. The vertical dashed lines correspond to the end of transducer activation.

Fig. 9 Temperature change as a function of time for the Pulse-Doppler mode: a) in Configuration #1, b) in Configuration #2. Location of the points is the same as in Figs. 8-a and -b. The vertical dashed lines correspond to the end of transducer activation

Fig. 10 Temperature change as a function of time for the SWE mode: a) in Configuration #1, b) in Configuration #2. Location of the points is the same as in Figs. 8-a and -b. The vertical dashed lines correspond to the end of transducer activation

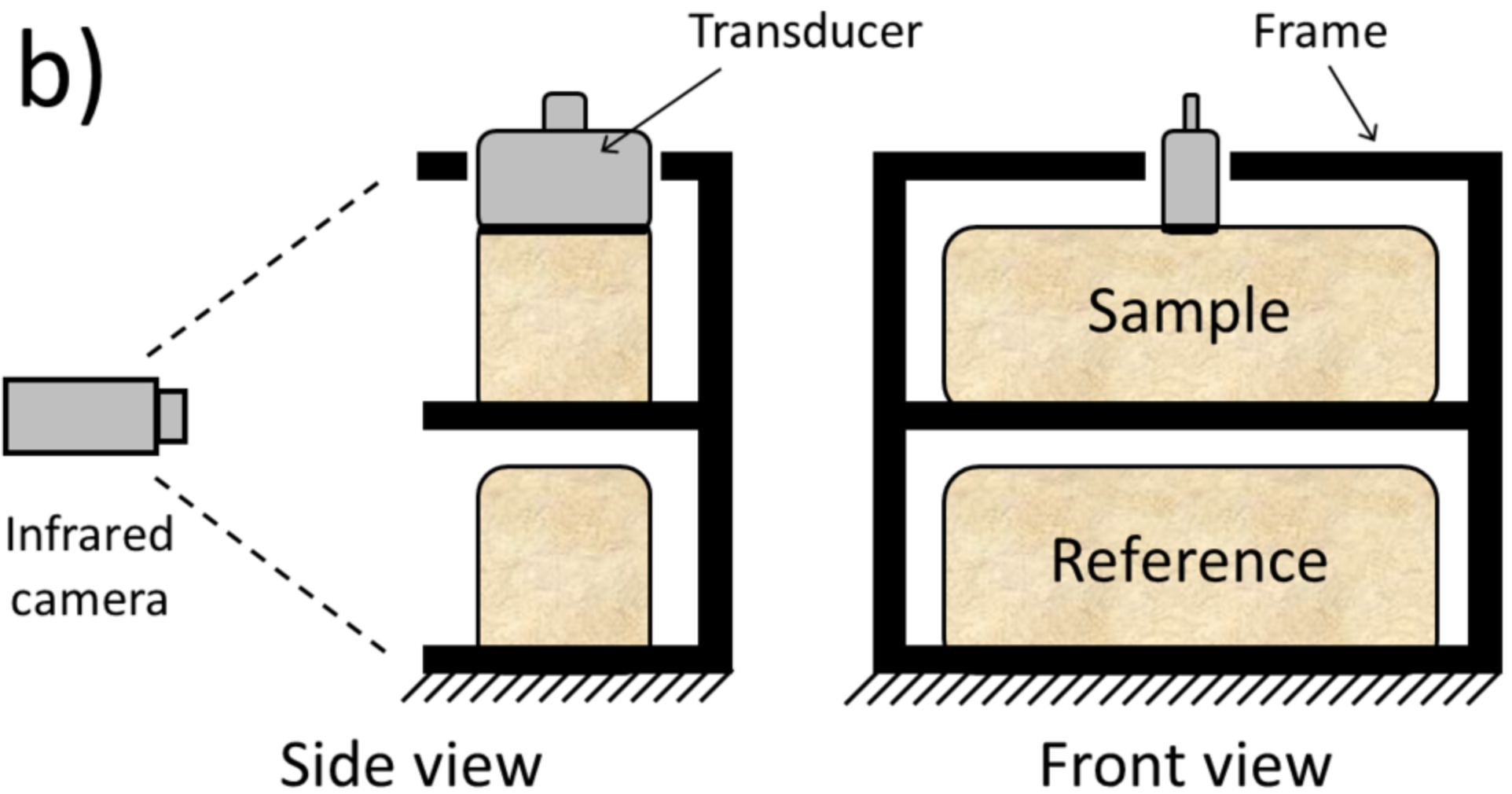
a)



Configuration #1

Configuration #2

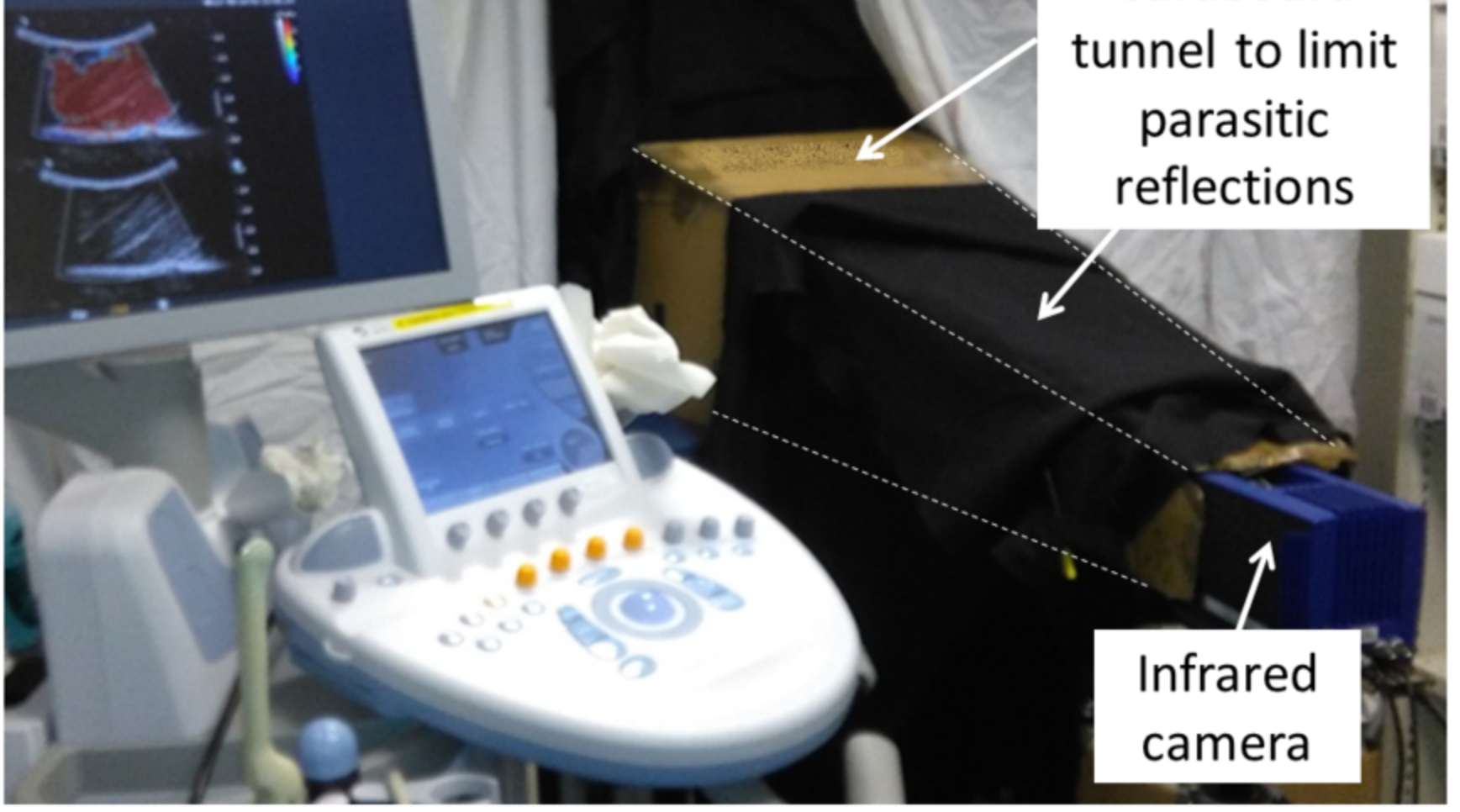
b)

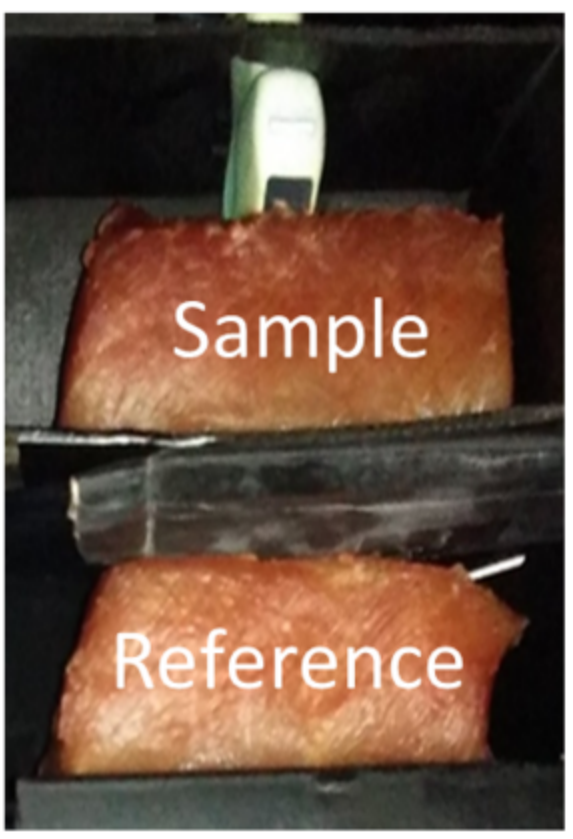


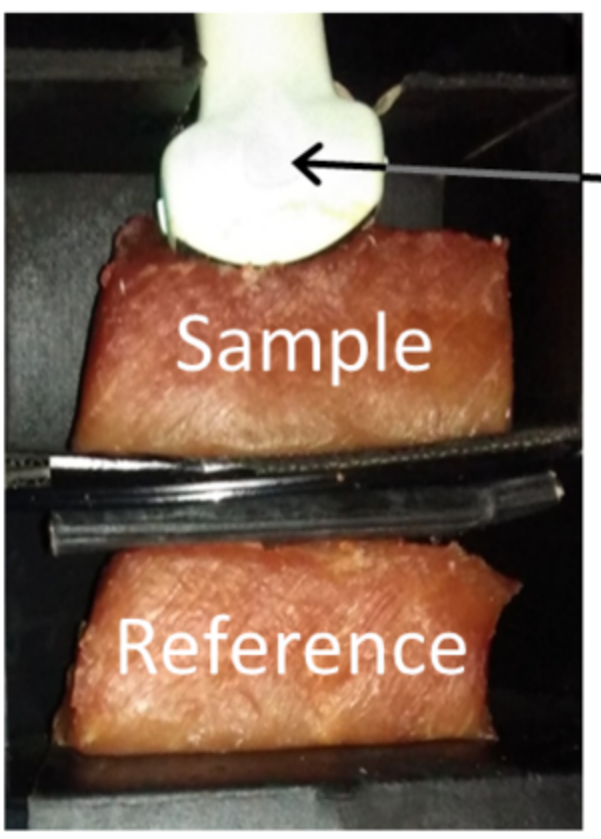
Side view

Front view

c)





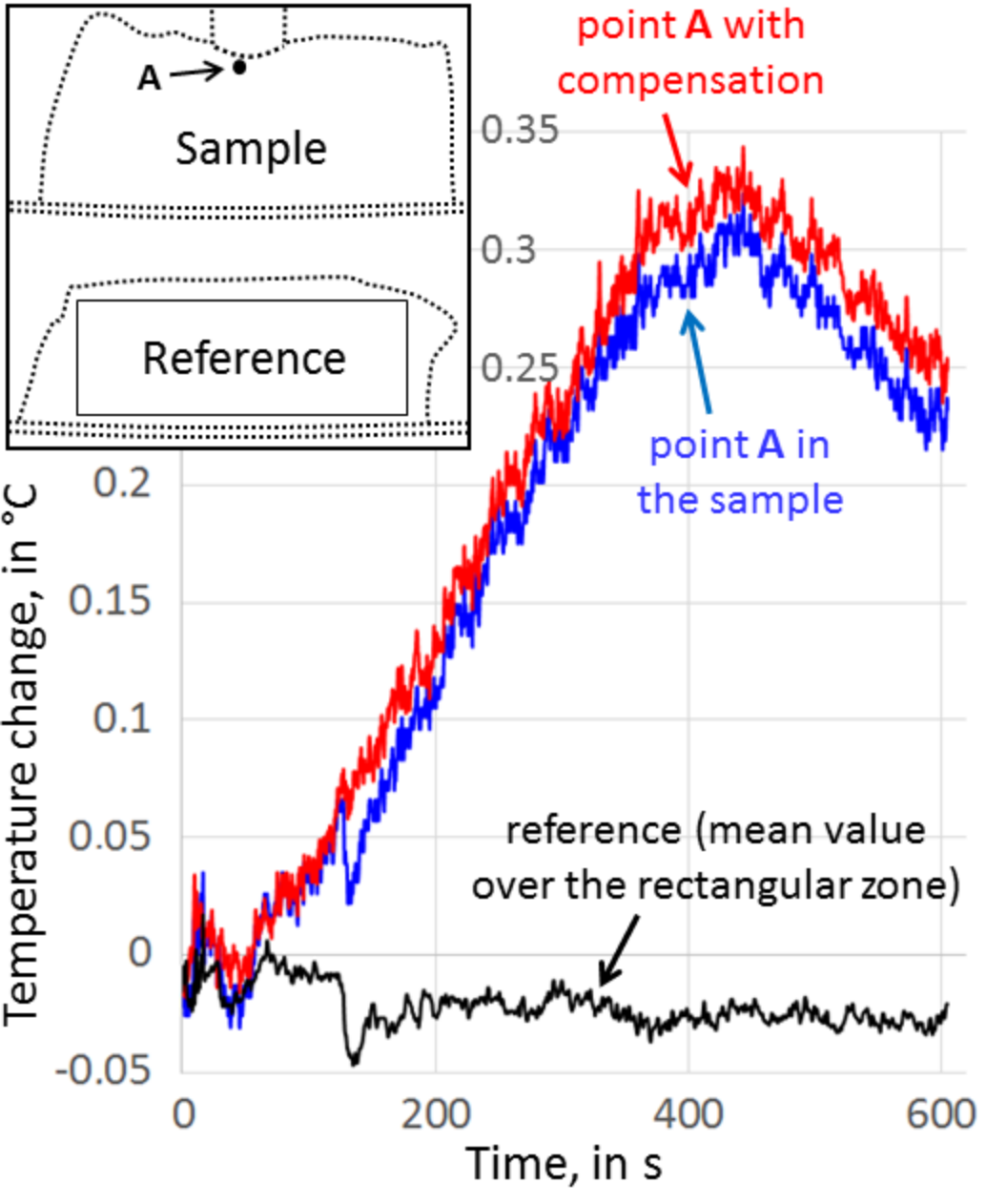


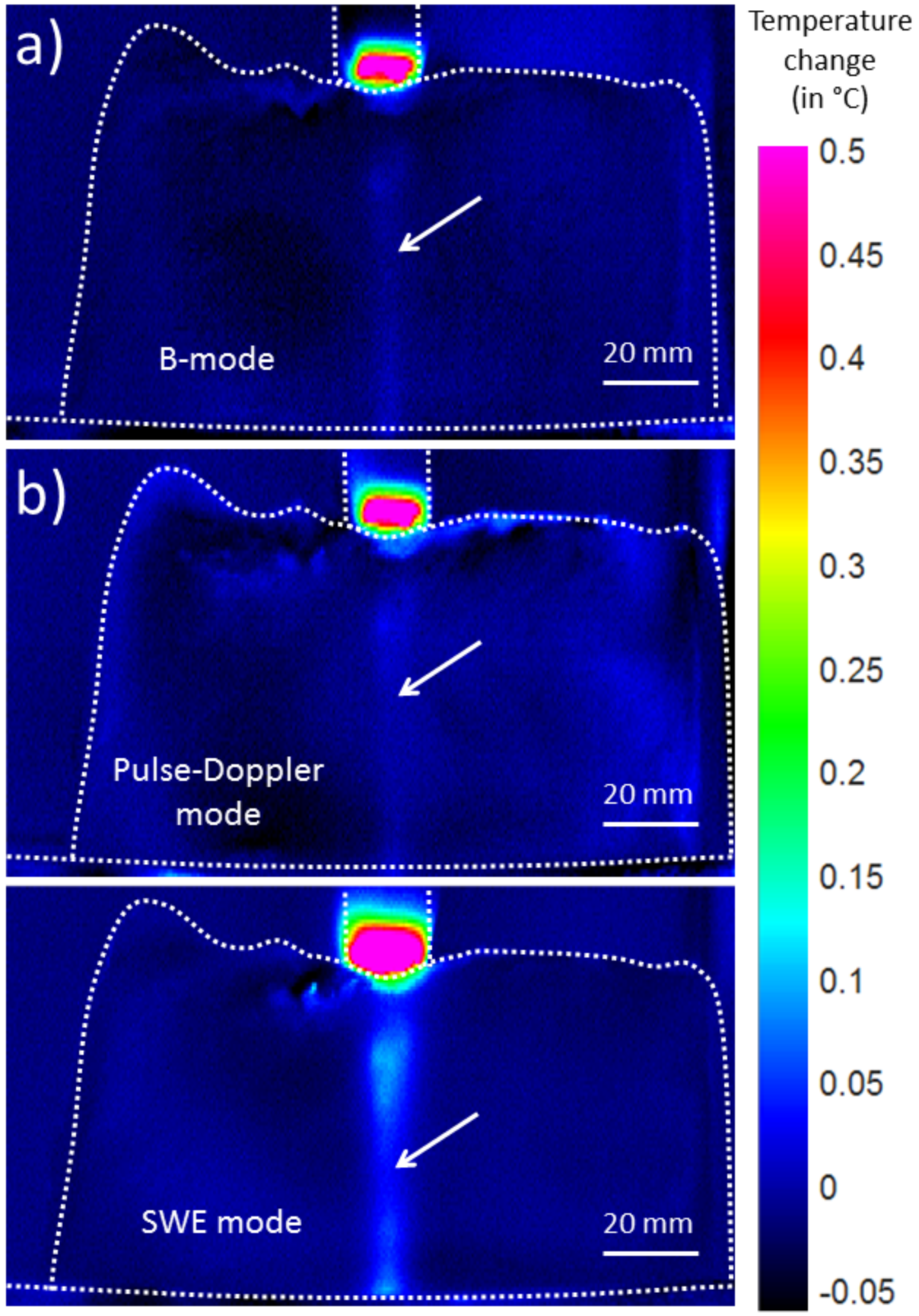
Curved transducer

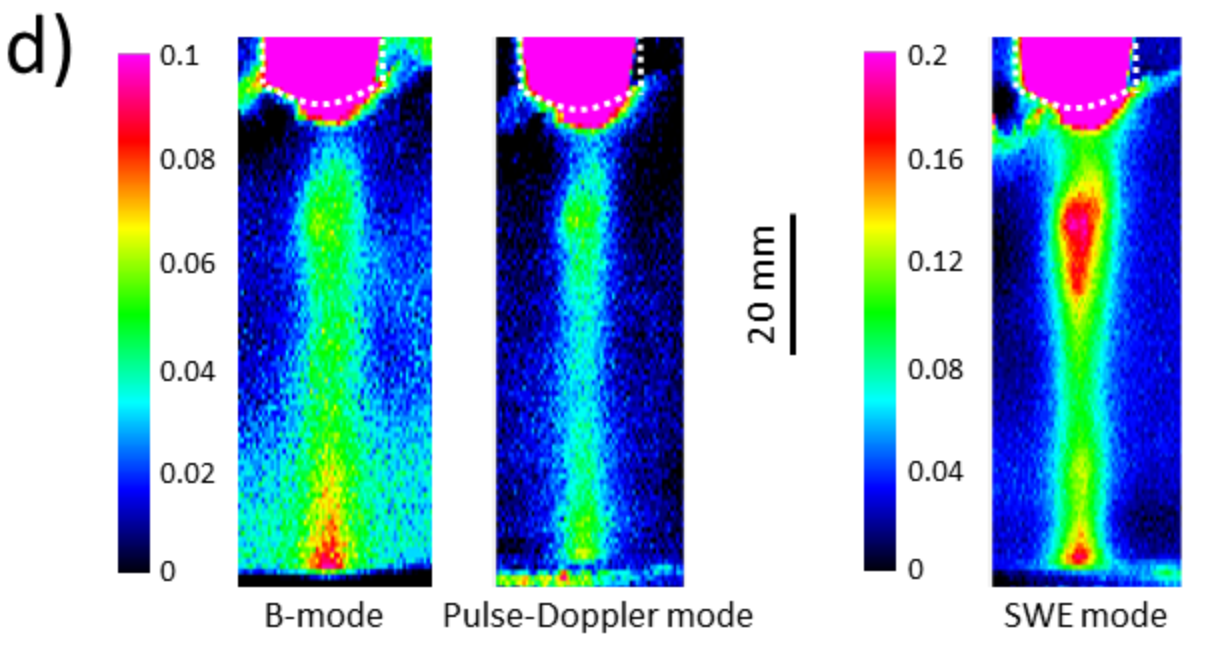
Closed environment, painted black to limit parasitic reflections

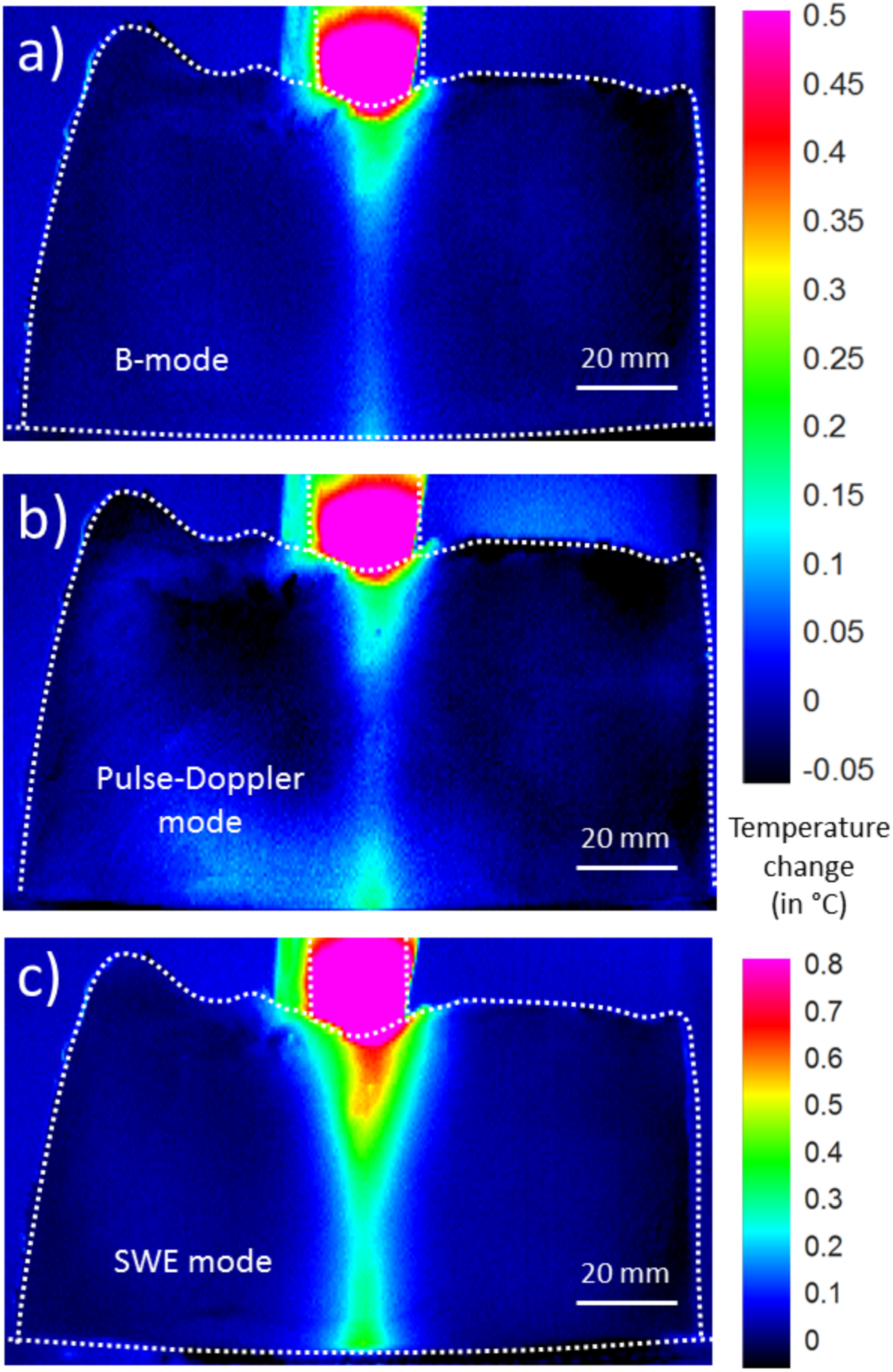
Configuration #1

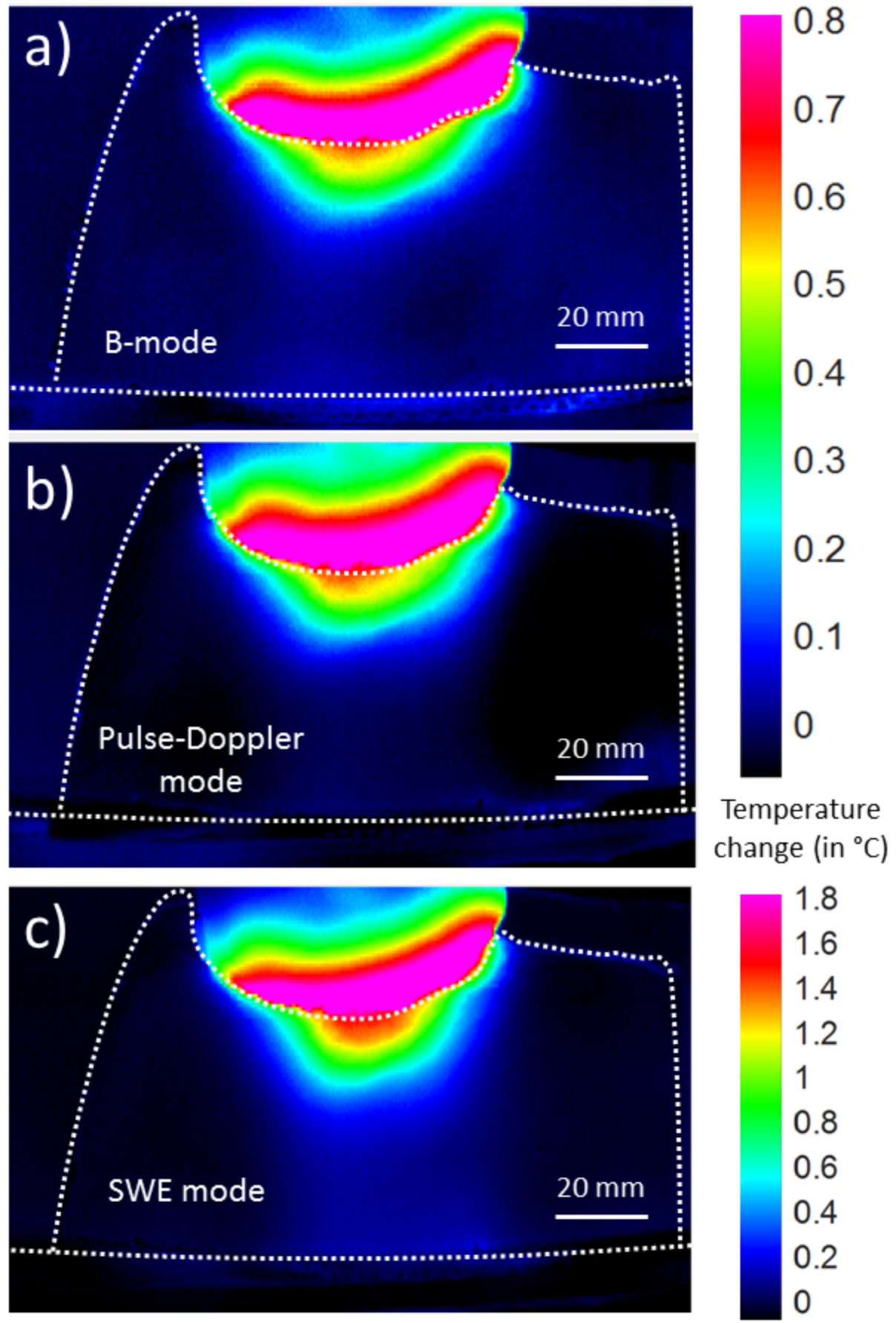
Configuration #2

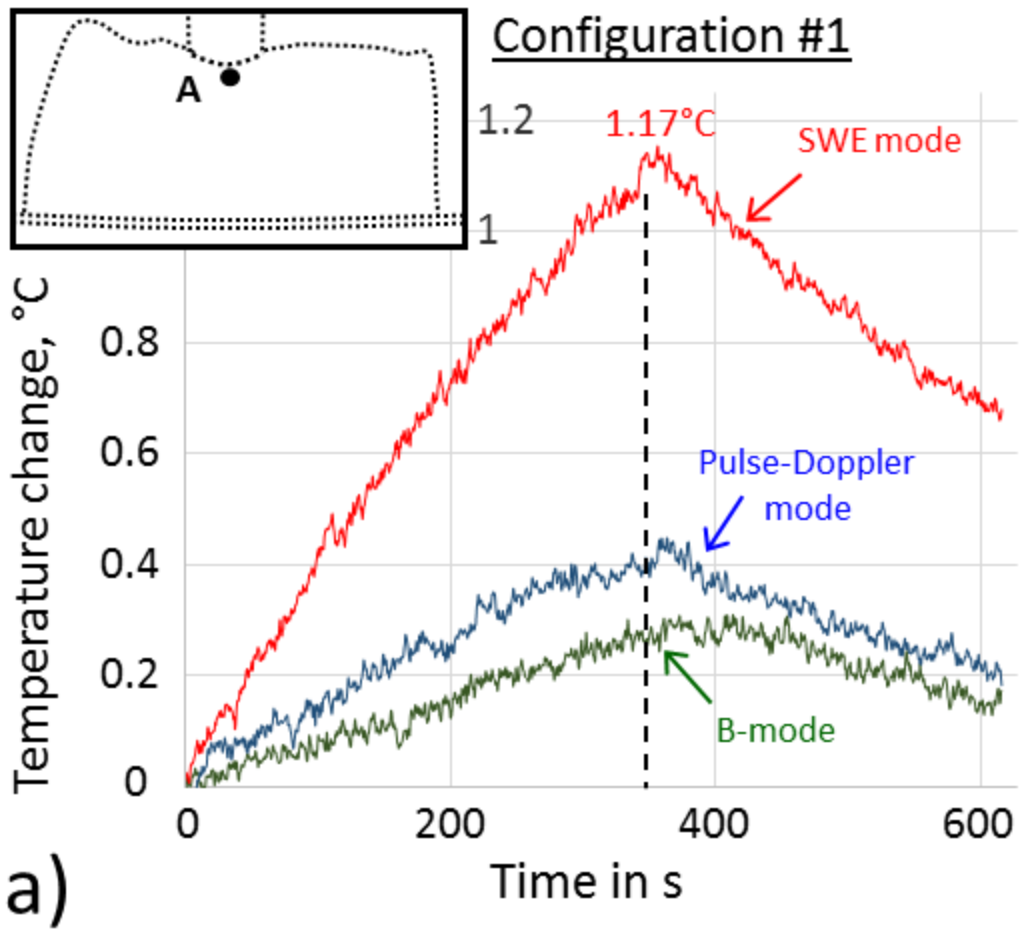

A
Sample
Reference
point A with compensation
point A in the sample
reference (mean value over the rectangular zone)
Temperature change, in °C
Time, in s
0.35
0.3
0.25
0.2
0.15
0.1
0.05
0
-0.05
0
200
400
600


a)
B-mode
20 mm
b)
Pulse-Doppler mode
20 mm
SWE mode
20 mm
Temperature change (in °C)
0.5
0.45
0.4
0.35
0.3
0.25
0.2
0.15
0.1
0.05
0
-0.05

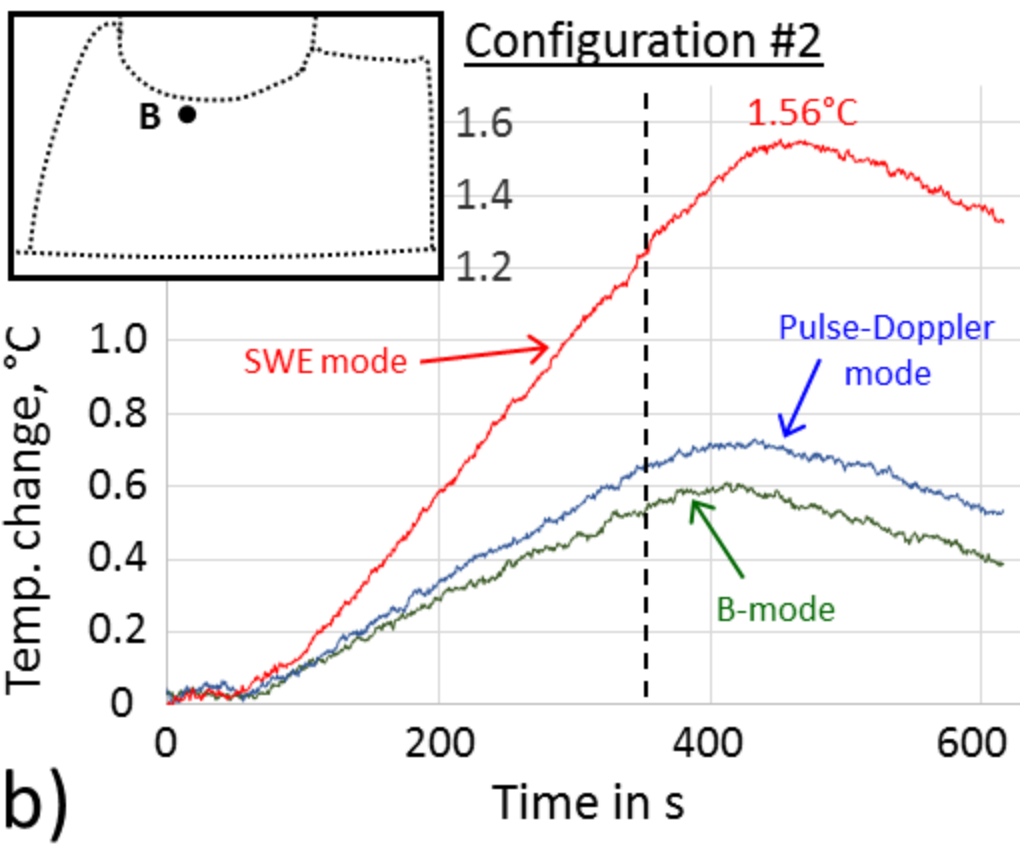

d)
0.1
0.08
0.06
0.04
0.02
0
20 mm
0.2
0.16
0.12
0.08
0.04
0
B-mode
Pulse-Doppler mode
SWE mode


a)
B-mode
20 mm
b)
Pulse-Doppler mode
20 mm
c)
SWE mode
20 mm
0.5
0.45
0.4
0.35
0.3
0.25
0.2
0.15
0.1
0.05
0
-0.05
Temperature change (in °C)
0.8
0.7
0.6
0.5
0.4
0.3
0.2
0.1
0

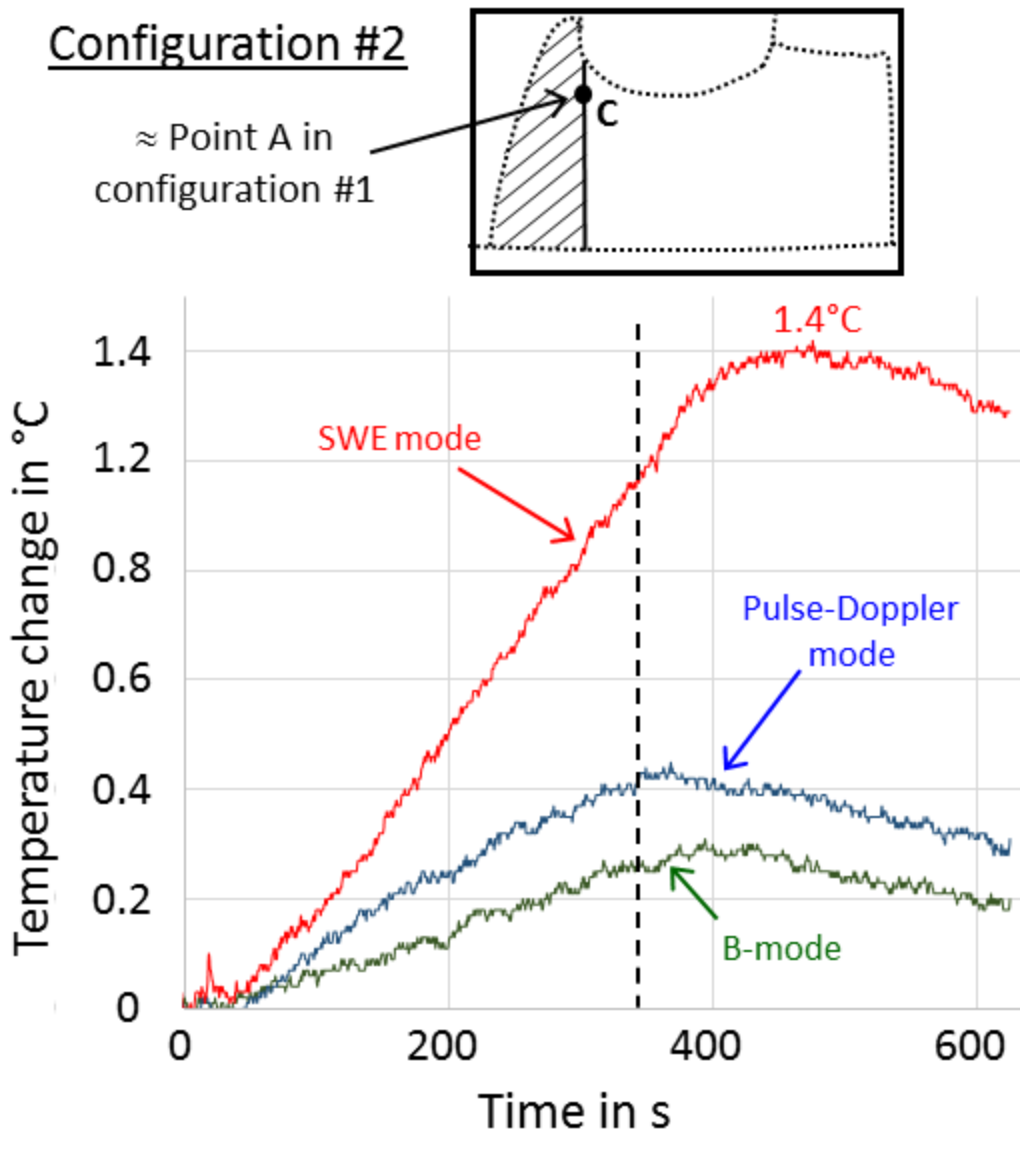

a)
B-mode
20 mm
b)
Pulse-Doppler mode
20 mm
c)
SWE mode
20 mm
0.8
0.7
0.6
0.5
0.4
0.3
0.2
0.1
0
Temperature change (in °C)
1.8
1.6
1.4
1.2
1
0.8
0.6
0.4
0.2
0

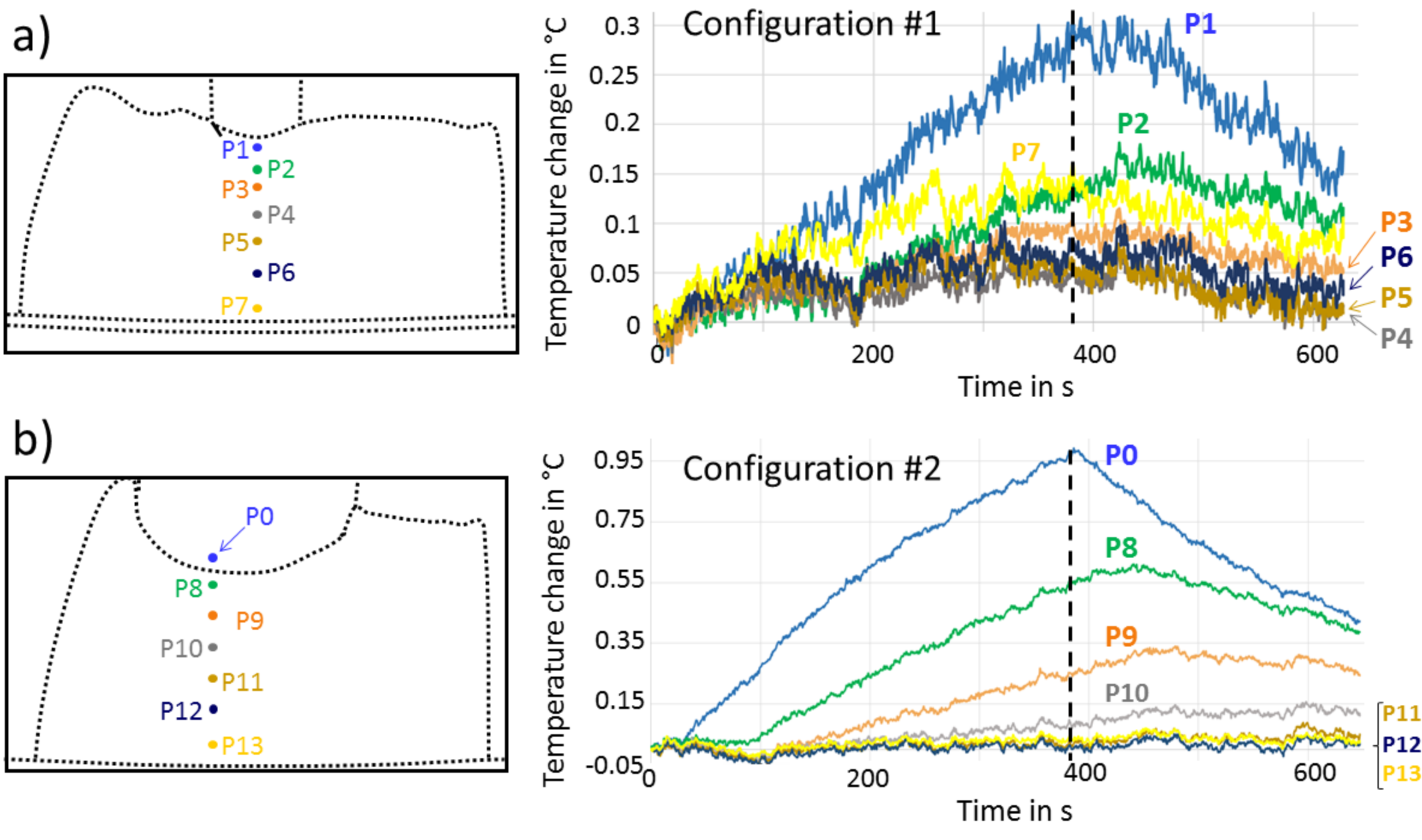

Configuration #1
A
1.17°C
SWE mode
Pulse-Doppler mode
B-mode
Temperature change, °C
Time in s
0
0.2
0.4
0.6
0.8
1
1.2
0
200
400
600

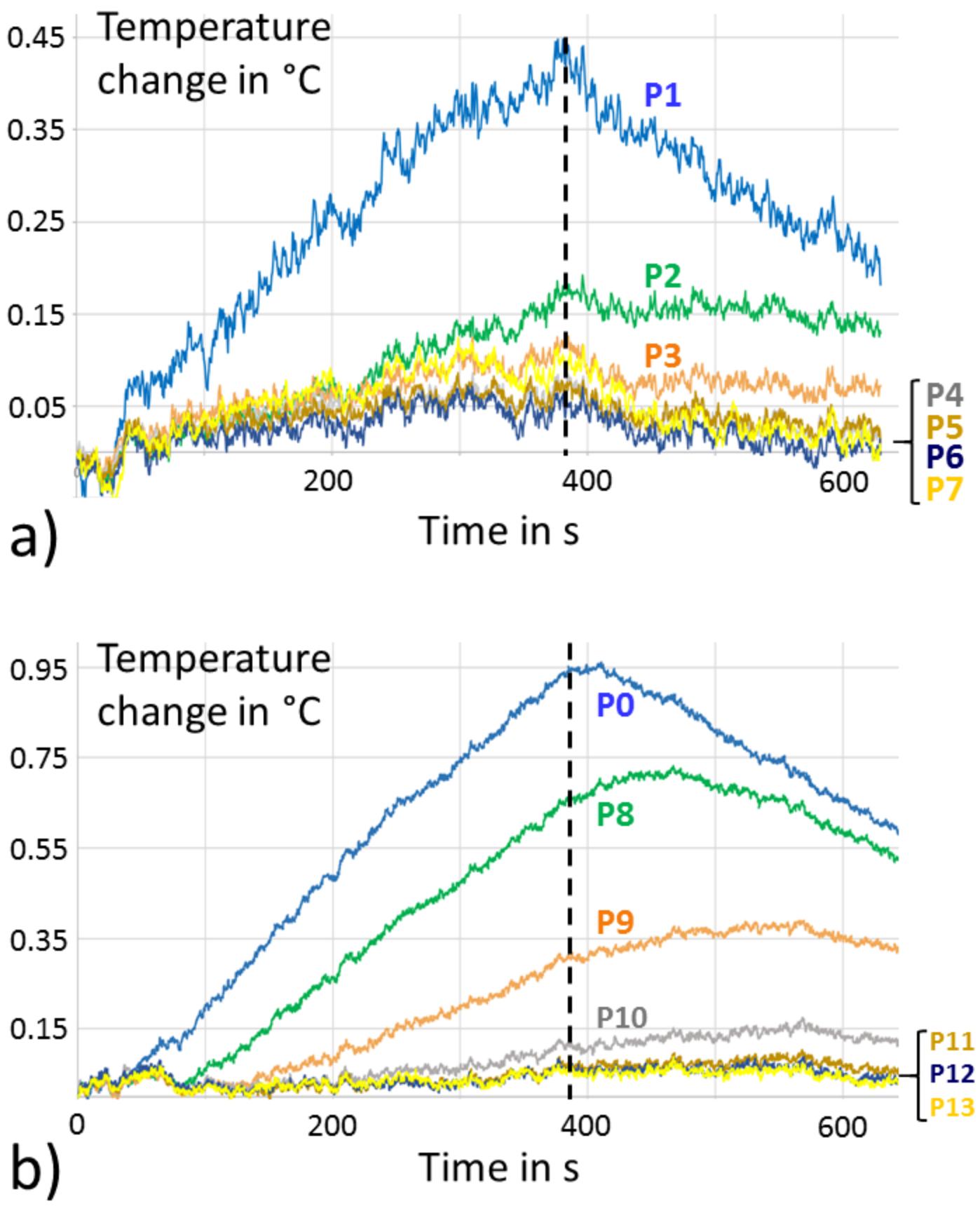
a)


Configuration #2
B
1.56°C
SWE mode
Pulse-Doppler mode
B-mode
Temp. change, °C
Time in s
0
0.2
0.4
0.6
0.8
1
1.2
1.4
1.6
0
200
400
600

b)


Configuration #2
≈ Point A in configuration #1
C
1.4°C
SWE mode
Pulse-Doppler mode
B-mode
Temperature change in °C
Time in s
0
0.2
0.4
0.6
0.8
1.2
1.4
0
200
400
600


a)
P1
P2
P3
P4
P5
P6
P7
Configuration #1
Temperature change in °C
0.3
0.25
0.2
0.15
0.1
0.05
0
0
200
400
600
Time in s
P1
P2
P7
P3
P6
P5
P4
b)
P0
P8
P9
P10
P11
P12
P13
Configuration #2
Temperature change in °C
0.95
0.75
0.55
0.35
0.15
-0.05
0
200
400
600
Time in s
P0
P8
P9
P10
P11
P12
P13


Temperature
change in °C
0.45
0.35
0.25
0.15
0.05
P1
P2
P3
P4
P5
P6
P7
200
400
600
Time in s
a)
Temperature
change in °C
0.95
0.75
0.55
0.35
0.15
P0
P8
P9
P10
P11
P12
P13
0
200
400
600
Time in s
b)

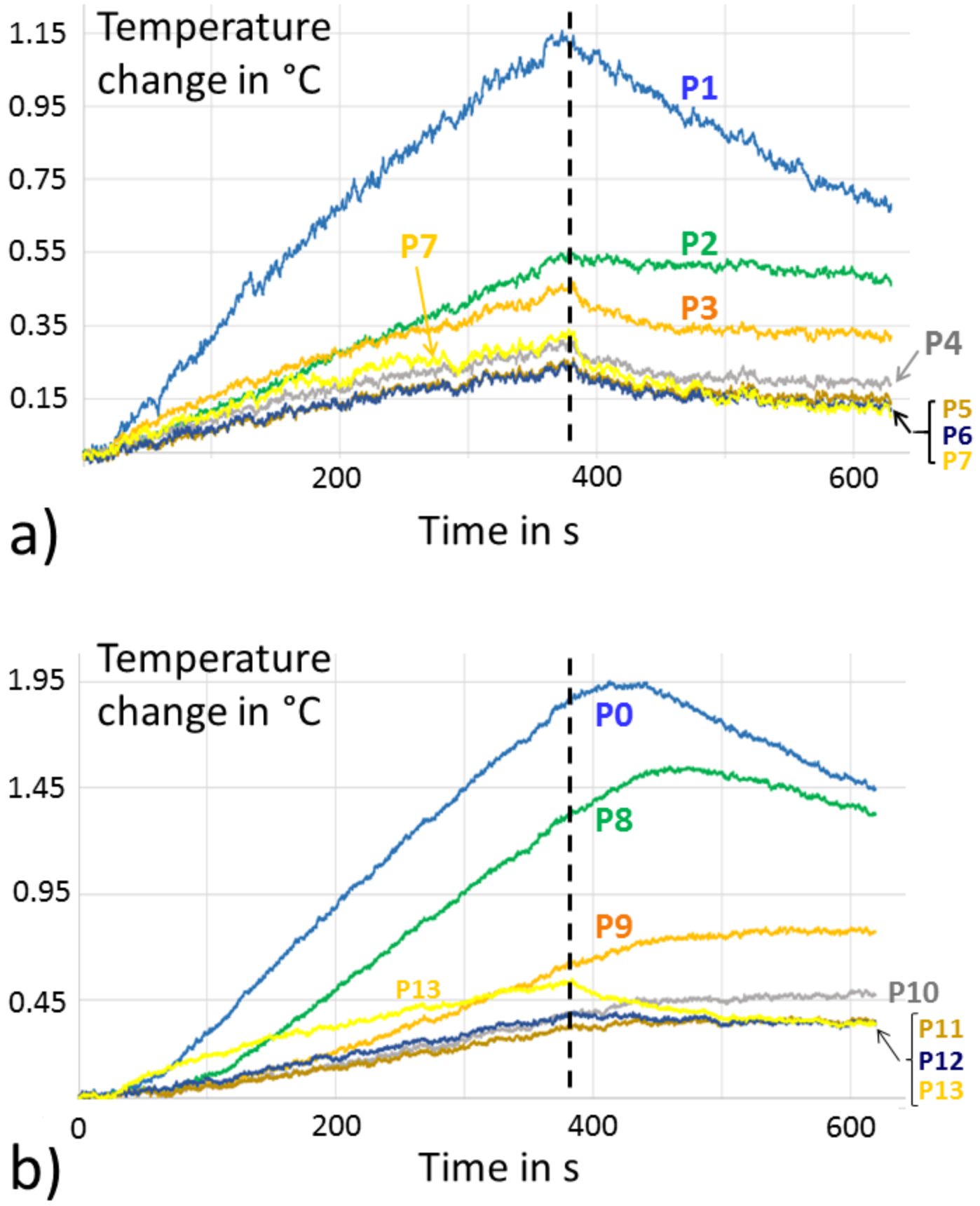

Temperature change in °C
1.15
0.95
0.75
0.55
0.35
0.15
P1
P2
P3
P4
P5
P6
P7
P7
200
400
600
Time in s
a)
Temperature change in °C
1.95
1.45
0.95
0.45
P0
P8
P9
P13
P10
P11
P12
P13
0
200
400
600
Time in s
b)

Table 1. Parameters for the three ultrasound modes used.

Parameters (OB-GYN GenOB preset)	B-mode	PD	SWE	Comment
Total depth	70 mm	22 mm	70 mm	
B-mode focal zone	10 – 25 mm	22 mm	25 – 40 mm	
Tissuetuner	1540 m/s	1540 m/s	1540 m/s	Speed of sound used to transmit and receive beamforming
SWE Opt (Res, Std, Pen)	N/A	N/A	Standard	Optimization of elastography resolution and penetration
SWE box geometry	N/A	N/A	Top width: 43.9 mm Bottom width: 63.2 mm Height: 30.8 mm Top depth: 6.7 mm	
MI	1.2	1	1.5	Mechanical Index
TIb	0	0	1.6	Thermal Index bone
TIs	0	0	1.4	Thermal Index soft tissue
Ispta	< 720 mW/cm^2	< 720 mW/cm^2	< 720 mW/cm^2	Spatial-peak temporal-average intensity